1174 Vol. 58, No. 4 / 1 February 2019 / Applied Optics Research Article

applied optics

Field stabilization control of the European Extremely Large Telescope under wind disturbance

KAINAN WANG AND ANDRÉ PREUMONT*

Department of Control Engineering and System Analysis, Université Libre de Bruxelles (ULB), CP. 165-55, 50 Av. F.D. Roosevelt, B-1050, Brussels, Belgium
**Corresponding author: andre.preumont@ulb.ac.be*

Received 27 August 2018; revised 11 December 2018; accepted 25 December 2018; posted 2 January 2019 (Doc. ID 343199); published 1 February 2019

This paper discusses the field stabilization control of the M5 unit under wind disturbances. The first part is a literature survey of the spectral content of the wind disturbance. Next, a simplified model of a tip/tilt mirror control system is used to analyze the conditions for control-structure interaction. The influence of the asymptotic decay rate of the wind tilt disturbance on the magnitude and spectral content of the control torques is pointed out. A full telescope model is developed to justify a decoupled tip/tilt control design and to analyze the response of the primary mirror M1 to the disturbance generated by the control torques of the M5 unit.

https://doi.org/10.1364/AO.58.001174

1. INTRODUCTION

Future extremely large telescopes require both improvements to the imaging resolution and enhancements to the field of view (FoV), which calls for complex multiple-mirror layouts and advanced adaptive optic (AO) systems. The 39 m European Extremely Large Telescope (E-ELT) proposes a novel five-mirror configuration design [1,2] where the deformable mirror (DM) M4 and the tip-tilt mirror (TTM) M5 are embedded within the main structure (Fig. 1) to compensate for high temporal frequency disturbances induced by atmospheric turbulence and wind buffeting. This built-in AO system exhibits more flexibility, simplifies the instrument complexity, and can be operated with other post-focal AO components (post-focal AO need to be duplicated at all foci) [3]. Other examples of built-in AO components can be found in the deformable secondary mirror of the Very Large Telescope UT4 [4], the adaptive secondary mirror module in the Large Binocular Telescope (LBT) [5], and in the adaptive secondary mirrors of the Giant Magellan Telescope (GMT) [6].

Despite the known benefits of embedded AO systems, the interaction between the AO control loop and the main structures should be a special concern, since the active components with large inertia (DM M4 and TTM M5) are attached mechanically to the telescope structure (unlike traditional lightweight AO mirrors in post-focal platforms), and the resonance frequencies of the telescope structure are significantly lower than those of smaller telescopes (the resonance frequencies scale according to $f_1 \sim D^{-1}$ [7]). When compensating for the external disturbances, the reactions of the control efforts excite the main structure and may introduce parasitic vibration sources that contaminate the wavefront. Figure 1 (right) gives a schematic view of the tip/tilt control loop and how the reaction torque is applied onto the main structure supporting M1. Notice the mechanical amplification by $I\omega^2$.

Another distinctive feature of E-ELT as compared to other smaller telescopes is that it will be a wind-limited telescope instead of a seeing-limited telescope. According to [8], "the reason is due to the fact that the wind facing the huge mechanical structure of the telescope itself produces a tip/tilt mode that is more than one order of magnitude larger than the atmospheric tilt." Figure 2 shows both the atmospheric and the wind tilt power spectral density (PSD) given in Ref. [8]. The corresponding root mean square (RMS) in arcsec on the sky are 1.003 arcsec for the wind and 0.0947 arcsec for the atmospheric turbulence. The decay rate of the atmospheric turbulence curve seems to agree with the results for the Z-tilt of [9] between 0.1 Hz and 1 Hz (see Fig. 6 of [9]; the high frequency decay rate is $-17/3$ and the corner frequency $f_c = 0.3(n+1)V/D = 0.15$ Hz with $n = 1$ (Z-tilt), $V = 10$ m/s, and $D = 40$ m), but the origin of the wind-shaking PSD is unknown to the authors; the surprisingly fast decay at frequencies above 1 Hz prompted the literature survey of the wind response spectra reported in the following section.

2. WIND DISTURBANCE SPECTRA

It is not clear how the wind disturbance PSD of Fig. 2 was obtained; the high frequency decay rate is of particular

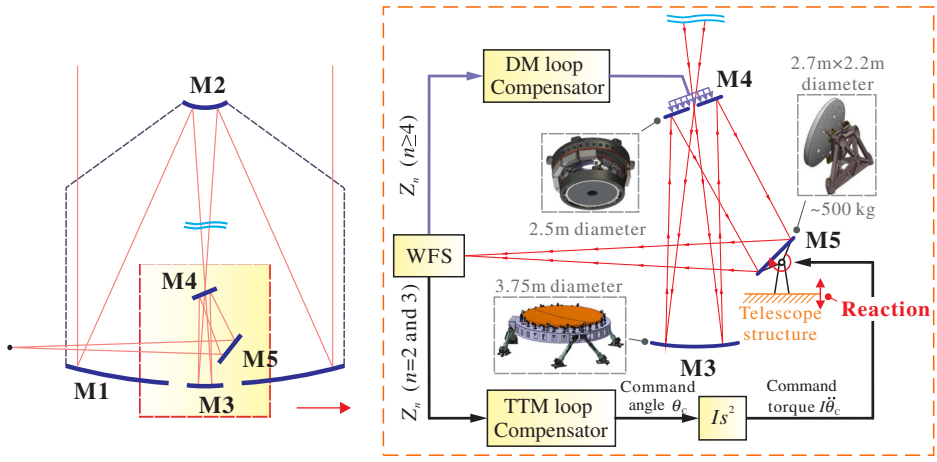

Fig. 1. Left, five-mirror configuration of the E-ELT telescope. Right, interaction of the tilt compensation control system with the telescope structure.

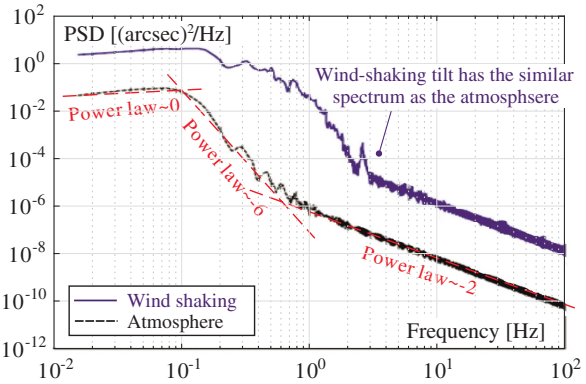

Fig. 2. PSD of the wind-shaking and the atmospheric tilt (from [8]).

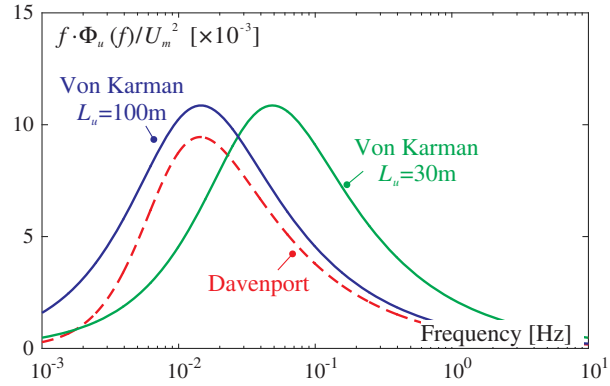

Fig. 3. PSD of the along wind turbulent velocity. Comparison of the von Karman (for $L_u = 100$ m and 30 m) and Davenport models.

importance because of the mechanical amplification of the reaction forces driving the high frequency components of the angular correction. This justifies a quick survey of the literature on wind buffeting. The most popular PSD models describing the turbulent wind velocity at a point are the von Karman spectrum, originally developed for airplane fatigue analysis, and the Davenport spectrum, based on meteorological data. The von Karman spectrum [10] assumes

$$\Phi_u(f) = \gamma^2 U_m^2 \frac{4L_u/U_m}{[1+70.7(L_u f/U_m)^2]^{5/6}}, \qquad (1)$$

where $\gamma = u_{\rm rms}/U_m$ is the turbulence intensity, ratio between the RMS turbulent velocity $u_{\rm rms}$, and the mean velocity U_m, and L_u is the turbulence eddy scale (average correlation length).

According to Davenport [11], the PSD of the turbulent velocity in the direction of the mean wind at one site may be represented by

$$\Phi_u(f) = \frac{4\kappa U_m^2}{f} \frac{(1200 f/U_m)^2}{[1+(1200 f/U_m)^2]^{4/3}}, \qquad (2)$$

where κ is a constant depending on the ground roughness, and U_m is the mean wind reference velocity 10 meters above the ground. The foregoing spectra are compared in Fig. 3, which shows $f\Phi_u(f)/U_m^2$ versus f in log scale [in this representation, the area of every frequency interval gives a fair image of the energy contained in this interval, since $f\Phi_u(f)d(\log f) = \Phi_u(f)df$]. The parameters used are as follows: the mean wind speed $U_m = 10$ m/s for both, the eddy scale $L_u = 30$ m (or 100 m), and the turbulence intensity $\gamma \simeq 0.2$ for von Karman model, the ground roughness constant $\kappa = 0.005$ for the Davenport model, which corresponds to the situation with open, unobstructed fields. Notice that the eddy size L_u strongly affects the power distribution in the von Karman model. Both models have a high frequency decay rate of −5/3. The telescope enclosure and the porous wind screens significantly reduce the mean wind velocity, but they tend to break the incoming vortices in smaller ones and shift the wind spectrum towards higher frequencies (reducing L_u). This wind velocity model was used in Ref. [12] to evaluate the disturbance torque on the elevation axis of radio telescopes.

The model above refers to the turbulent velocity at one point. If the turbulent velocity is small with respect to the mean wind $u \ll U_m$, the model can be used to describe the pressure distribution. An asymptotic decay rate of −7/3 instead of −5/3

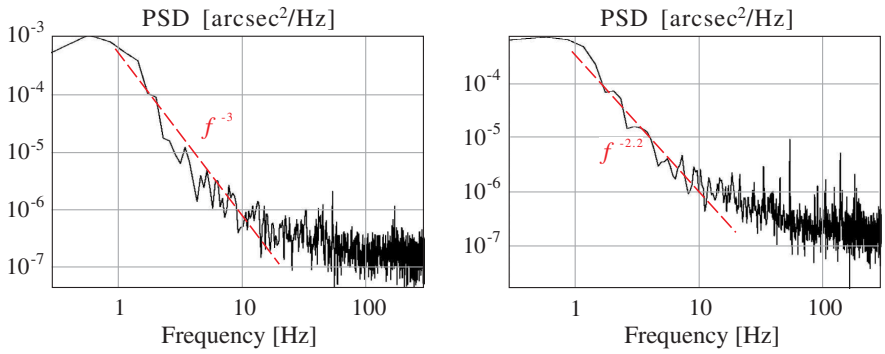

Fig. 4. PSD of the optical tilt measured by a natural guide star at the Gemini South 8 m telescope (from [20]). The tip/tilt PSDs exhibit a roll-off rate of 3 and 2.2, respectively, in the frequency band 1–10 Hz.

has been suggested to account for the second-order term of the velocity in the pressure distribution [13]. This frequency dependency of the wind pressure at one point has been confirmed by pressure measurements on the primary mirror of the Gemini telescope with ventilation gates open [14].

The spatial coherence plays a crucial role in the wind response of very large structures, because the forces acting on the various parts of the structure are gradually uncorrelated as the distance between these parts grows. To account for this, the telescope literature [13,15–17] suggests (the origin of this correction seems to be [18]) to multiply the wind velocity spectrum by the function

$$\chi_a^2(f) = \frac{1}{[1 + (2f\sqrt{A}/U_m)^{4/3}]^2}, \tag{3}$$

where A is the area facing the wind and U_m is the mean velocity. Thus, the overall asymptotic decay rate is $-5/3 - 8/3 = -13/3$ (instead of $-17/3$ for the atmospheric tilt [9]).

Davenport [11] suggests the following expression for the coherence in the vertical direction:

$$\Psi(\Delta z, f) = \exp\left(-\frac{Cf}{U_m}\Delta z\right), \tag{4}$$

with $C = 7$; Δz is the vertical distance between the two points. An analytical random vibration study on a one-dimensional structure with various boundary conditions [19] shows that the generalized forces acting on the structure (called *acceptance functions* in the random vibration vocabulary) exhibit an additional decay rate of -1 above a corner frequency given approximately by

$$\frac{CL}{U_m} \cdot f > 10, \tag{5}$$

where L is the characteristic length of the structure. Using $C = 7$, $L = 40$ m, and $U_m = 10$ m/s leads to $f > 0.35$ Hz. Thus, in the case of the wind response of a tall, slender structure, the overall roll-off rate at high frequency becomes $-5/3 - 1 = -8/3$. We conducted numerical simulations on large two-dimensional structures with a square shape, assuming an isotropic coherence of the form of Eq. (4), where Δz is now the distance separating two points; the study is summarized in Appendix A, and the results indicate that the asymptotic decay rate of the acceptance functions is the same for all boundary conditions. For a rigid body mode, it can be shown analytically that it converges asymptotically to -2; this leads to an overall decay rate of $-5/3 - 2 = -11/3$.

Finally, it is worth mentioning the open-loop Natural Guide Star (NGS) observations at the 8 m Gemini South [20], which exhibit a roll-off rate between 2 and 3 in the frequency range 1–10 Hz (Fig. 4).

To summarize this section, there seems to be a significant uncertainty on the asymptotic decay rate of the wind disturbance, between $f^{-2.2}$ (NGS, Gemini South, Fig. 4) and $f^{-13/3}$ [13,15–17]. Its impact on the disturbance torque applied to the primary structure will be investigated below.

3. FEEDBACK CONTROL OF THE TIP-TILT MIRROR

The block diagram of the field stabilization (TTM) loop is shown in Fig. 5. Since the large TTM mirror is supported by the telescope structure, its control actuators will act as a disturbance to the main telescope structure, affecting the image quality. Also, the flexibility of the telescope structure may have a destabilizing effect on the TTM control loop.

A. Control-Structure Interaction Model

Consider the two-degree-of-freedom (d.o.f) system of Fig. 6; the subscript s refer to the structure, and the subscript a refers to the active mirror (the TTM in this case). If the mirror is actuated piezoelectrically, $F_a = k_a\Delta$, where Δ is the free piezoelectric expansion of the actuator (proportional to the voltage applied). Both mirrors affect the wavefront sensor (WFS) y according to

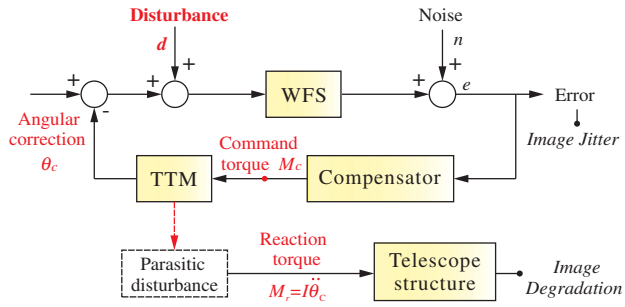

Fig. 5. Block diagram of the field stabilization loop generating a parasitic disturbance to the telescope structure.

$$y = x_s + \frac{D_a}{D_s} x_a = x_s + \delta x_a, \tag{6}$$

where $\delta = D_a/D_s$ is the diameter ratio. If the mass ratio $\varepsilon = m_a/m_s \ll 1$, the mode shapes are shown in Figs. 6(b) and 6(c), with natural frequencies

$$f_1 \approx \frac{f_s}{\sqrt{1+\varepsilon}} \quad \text{and} \quad f_2 \approx f_a\sqrt{1+\varepsilon},$$

where $f_s = \frac{1}{2\pi}\sqrt{k_s/m_s}$ is the natural frequency of the structure alone and $f_a = \frac{1}{2\pi}\sqrt{k_a/m_a}$ is the natural frequency of the active mirror. It is simple to establish that the open-loop transfer function reads (see Appendix B)

$$\frac{y}{F_a} = \frac{y}{k_a\Delta} = \frac{-m_a s^2 + \delta(m_s s^2 + c_s s + k_s)}{[m_s s^2 + (c_s + c_a)s + (k_s + k_a)](m_a s^2 + c_a s + k_a) - (c_a s + k_a)^2}. \tag{7}$$

Thus, the undamped open-loop imaginary zeros $\pm jz_1$ are solutions of

$$-m_a s^2 + \delta(m_s s^2 + k_s) = 0,$$

leading to

$$z_1^2 = \frac{\delta}{\delta - \varepsilon} f_s^2 = \frac{\delta(1+\varepsilon)}{\delta - \varepsilon} f_1^2. \tag{8}$$

The frequency of the zeros is close and slightly higher than that of the first poles; the relative spacing reads

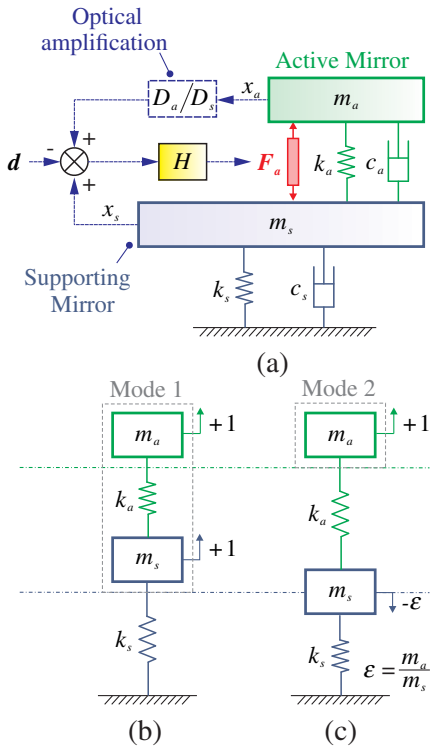

Fig. 6. (a) Two-d.o.f. system. The mass m_s and the displacement x_s refer to the telescope structure supporting the primary mirror of diameter D_s; m_a and x_a refer to the TTM of diameter D_a. The sensor output reads $y = x_s + (D_a/D_s)x_a$. (b) and (c) Mode shapes; $\varepsilon = m_a/m_s$. For a piezoelectric actuator, $F_a = k_a\Delta$, where Δ is the free actuator expansion.

$$Q = \frac{z_1 - f_1}{f_1} = \sqrt{\frac{\delta(1+\varepsilon)}{\delta - \varepsilon}} - 1, \tag{9}$$

where $\varepsilon = m_a/m_s$ is the mass ratio and $\delta = D_a/D_s$ is the optical amplification. If $\delta = 1$,

$$Q = \sqrt{\frac{1+\varepsilon}{1-\varepsilon}} - 1 \approx \varepsilon. \tag{10}$$

Thus, in absence of optical amplification, Q is simply the mass ratio. If one takes into account the structural damping, there is a closely spaced pole-zero pair in the vicinity of f_1 that is responsible for a "notch" in the phase diagram (Fig. 7). The phase lag in the frequency range between f_1 and z_1 reads

$$\theta = \theta_p - \theta_z = 180° - \arctan\left(\frac{2\xi f_1 f}{f^2 - f_1^2}\right) - \arctan\left(\frac{2\xi z_1 f}{z_1^2 - f^2}\right), \tag{11}$$

where $\xi = c_s/(2\pi f_s m_s)$ is the fraction of critical damping of the supporting mirror. The maximum phase lag occurs at $f = \sqrt{f_1 z_1}$ and, after substituting in the foregoing equation,

$$\theta_{\max} = \theta_p - \theta_z = 180° - 2\arctan\left(\frac{2\xi\sqrt{Q+1}}{Q}\right) \approx 180° - 2\arctan\left(\frac{2\xi}{Q}\right) \tag{12}$$

if Q is small.

B. Stability Analysis

Figure 7 shows the open-loop transfer function $G(f)H(f)$ if an integral compensator is assumed, $H(f) = f_c/jf = -jf_c/f$, for a value of the crossover frequency f_c below the first mode at f_1. A value of $Q = 0.007$ and a damping ratio of $\xi = 0.01$ have been assumed for illustration. The left side of the figure shows the Bode plot, while the Nichols plot is shown on the right side. Note that, when f_c increases, the phase diagram is unchanged, and the Nichols plot is simply translated upwards along the amplitude axis. Two types of instability are possible:

- The most classical one, associated with the actuator mode at f_2. The stability condition is $f_2/f_c > 1/2\xi_2$, and the gain margin is

$$\text{GM} = 20\log\left[\frac{2\xi_2 f_2}{f_c}\right]. \tag{13}$$

- The second one is associated with the structure mode f_1. A phase margin larger than PM is guaranteed if the maximum phase lag associated with the pole-zero pair satisfies

$$\theta_{\max} = 180° - 2\arctan\left(\frac{2\xi_1}{Q}\right) \le 90° - \text{PM}. \tag{14}$$

For example, assuming $\xi_1 = 0.01$, a phase margin larger to PM = 45° will always be guaranteed, irrespective of the bandwidth (defined by f_c) provided $Q \le 8.3 \times 10^{-3}$. Using E-ELT data for M1 an M5 as order of magnitude, $m_s = 1.5 \times 10^6$ kg, $D_s = 40$ m, $m_a = 500$ kg, $D_a = 2.5$ m, one gets $Q = 2.8 \times 10^{-3}$, well below the threshold. If a Butterworth filter

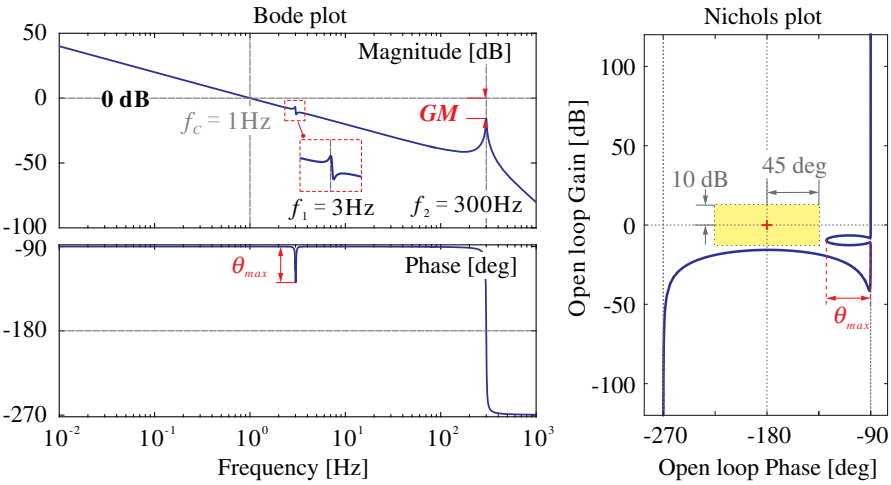

Fig. 7. Open-loop transfer function $G(f)H(f)$ if an integral control is assumed ($Q = 0.007$, $f_c = 1$ Hz, $f_1 = 3$ Hz, $f_2 = 300$ Hz). Left, Bode amplitude and phase plot. Right, Nichols plot. There is a closely spaced pole-zero pair near f_1.

with corner frequency f_b is added to increase the roll-off rate at high frequency, some phase shift depending on the ratio f_1/f_b will be added to $\theta_{\max}$.

C. Disturbance Rejection

Our objective is to study the uncertainty associated with the roll-off rate of the wind tilt disturbance, rather than optimizing the control law. Referring to Fig. 5, the WFS is assumed to have perfect dynamics and be noiseless; the disturbance d assumes one of the forms shown in Fig. 8 (all normalized to a RMS value of 1 arcsec). The control objective is to reduce the RMS response to 0.07 arcsec. The compensator is assumed to be an integrator plus a second-order Butterworth filter with a corner frequency ω_b as follows:

$$H(s) = \frac{g}{s} \cdot \frac{\omega_b^2}{s^2 + \sqrt{2}\omega_b s + \omega_b^2}. \tag{15}$$

In order to use the simple model of Fig. 6 with angular coordinates rather than translational ones, it is convenient to rewrite Eq. (7) with the notations $\omega_s^2 = k_s/m_s$ and $\omega_a^2 = k_a/m_a$ as follows:

$$G(s) = \frac{y}{\Delta} = \frac{\omega_a^2[-\varepsilon s^2 + \delta(s^2 + 2\xi_s\omega_s s + \omega_s^2)]}{[s^2 + 2\xi_s\omega_s s + \omega_s^2 + \varepsilon\omega_a^2][s^2 + 2\xi_a\omega_a s + \omega_a^2] - (\omega_a^2 + 2\xi_a\omega_a s)^2\varepsilon}. \tag{16}$$

If the control-structure interaction is neglected, $\varepsilon = 0$; in this case, $G(s)$ reads

$$G(s) = \frac{y}{\Delta} = \delta \cdot \frac{\omega_a^2}{s^2 + 2\xi_a\omega_a s + \omega_a^2}. \tag{17}$$

Thus, the crossover frequency of $G(s)H(s)$ is $\omega_c = g\delta$. In this study, the corner frequency of the Butterworth filter has been taken as $\omega_b = 10g\delta$. For E-ELT, $m_a = 500$ kg and $m_s = 1.5 \times 10^6$ kg, $\varepsilon = m_a/m_s = 3.3 \times 10^{-4}$; for this small value of ε, the results are not affected by the control-structure interaction.

According to feedback theory, the output y and the disturbance d are related by the sensitivity function T as follows:

$$y = \frac{1}{1 + GH} \cdot d = T \cdot d. \tag{18}$$

The PSD of the residual tilt is obtained from the disturbance PSD $\Phi_d(f)$ according to

$$\Phi_y(f) = \Phi_d(f) \cdot |T(f)|^2, \tag{19}$$

and the RMS residual error reads

$$\sigma_e = \left[\int_0^\infty \Phi_d(f) \cdot |T(f)|^2 \mathrm{d}f\right]^{1/2}. \tag{20}$$

Figure 9 shows the evolution of the residual RMS tilt error as a function of the control bandwidth for the various PSDs assumed in Fig. 8. One sees that the control bandwidth (measured here by the crossover frequency f_c) necessary to achieve the control objective of a residual tilt of $\sigma_e = 0.07$ arcsec with the compensator of Eq. (15) varies considerably, from $f_c = 4.6$ Hz if the asymptotic decay rate is $-13/3$ to $f_c = 13.3$ Hz if a decay rate of $-8/3$ is assumed (notice that, in all cases, $f_c > f_1 = 3$ Hz).

For the three values of the asymptotic decay rate of respectively $-8/3$, $-11/3$, and $-13/3$ and the control bandwidth leading to a residual RMS wind tilt error of 0.07 arcsec, Fig. 10 shows the PSD of the control input Δ, the free expansion of the piezoelectric actuator (proportional to the voltage applied) as

$$\Delta = H(s) \cdot y, \tag{21}$$

where $H(s)$ is the compensator, Eq. (15) in this case. Thus,

$$\Phi_\Delta(f) = \Phi_y(f) \cdot |H(f)|^2. \quad (22)$$

The total reaction force applied to the support structure is the sum of the actuator force $k_a\Delta$ and the forces transmitted by the spring k_a and the damper c_a. Overall, with the notations of Fig. 6, it is given by $-m_a\ddot{x}_a$. The transfer function between x_a and Δ is easily found to be

$$G_a(s) = \frac{x_a}{\Delta} = \frac{\omega_a^2(s^2 + 2\xi_s\omega_s s + \omega_s^2)}{[s^2 + 2\xi_s\omega_s s + \omega_s^2 + \varepsilon\omega_a^2][s^2 + 2\xi_a\omega_a s + \omega_a^2] - (\omega_a^2 + 2\xi_a\omega_a s)^2\varepsilon}. \quad (23)$$

Thus, the disturbance torque M_s applied to the main structure of the telescope is given by

$$M_s = -I_a s^2 G_a(s) H(s) y, \quad (24)$$

where the moment of inertia I_a of the TTM mirror is used instead of the mass m_a appearing in the model of Fig. 6.

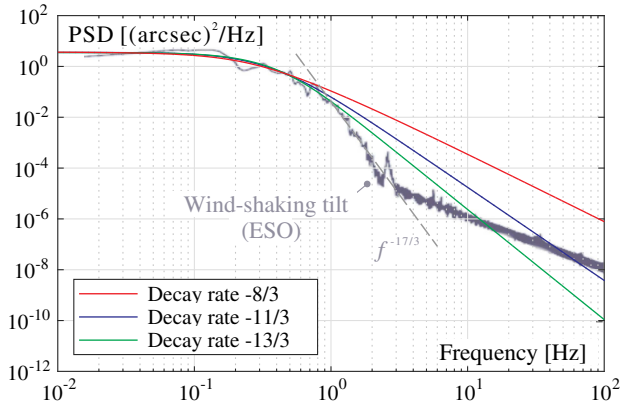

Fig. 8. Wind tilt disturbance PSD assumed in the parametric study. All PSDs are normalized to a RMS value of 1 arcsec; the exponent of asymptotic decay rate varies from −8/3 to −13/3. The wind shake tilt PSD from [8] is also shown in the background.

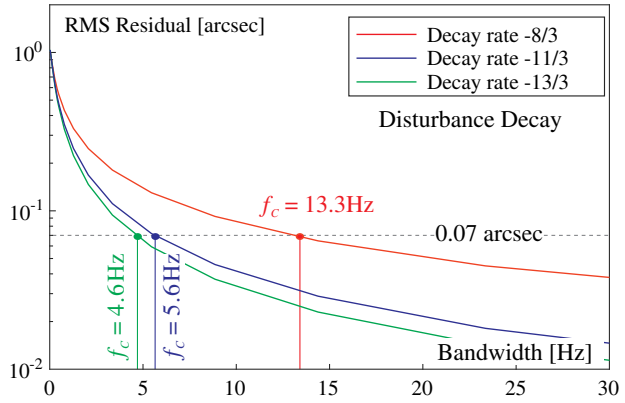

Fig. 9. Evolution of the residual RMS error σ_e with the crossover frequency f_c for the various assumptions on the asymptotic decay rate of the wind tilt disturbance. The control objective is to reduce the residual tilt to 0.07 arcsec RMS.

Figure 11 shows, for the same three cases considered in Fig. 10, the PSD of the TTM rotational acceleration $\ddot{x}_a$.

Because the control variable is the tilt angle of the TTM mirror, while the disturbance torque M_s applied to the telescope structure depends on the angular *acceleration*, there is a considerable amplification ($\sim f^4$) of the high frequency components in $\Phi_{\ddot{x}_a}(f)$, as compared to the control itself, $\Phi_\Delta(f)$.

Table 1 summarizes the results; it gives the control bandwidth (the crossover frequency f_c), the RMS tilt acceleration

$$\sigma_0 = \left[\int_0^\infty \Phi_{\ddot{x}_a}(f)\mathrm{d}f\right]^{1/2}, \quad (25)$$

and the central frequency defined by the *Rice formula*

$$f_0 = \left[\frac{\int_0^\infty f^2\Phi_{\ddot{x}_a}(f)}{\int_0^\infty \Phi_{\ddot{x}_a}(f)\mathrm{d}f}\right]^{1/2} \quad (26)$$

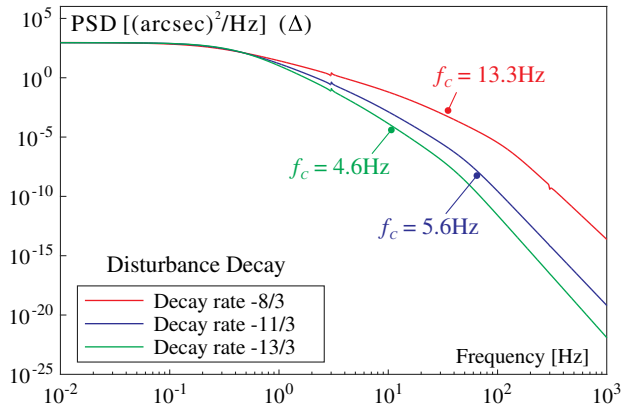

Fig. 10. PSD of the control Δ for three values of the asymptotic decay rate of the wind tilt disturbance and the control bandwidth leading to a residual RMS tilt error of 0.07 arcsec.

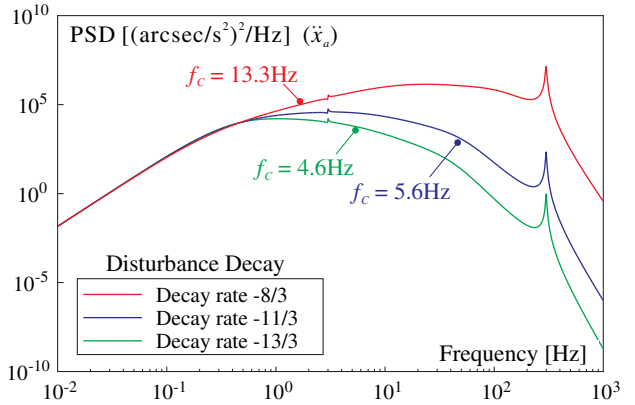

Fig. 11. PSD of the TTM angular acceleration for the three cases considered in Fig. 10 in order to achieve a residual RMS tilt of 0.07 arcsec.

Table 1. Control Bandwidth f_c, RMS Tilt Acceleration σ_0, and Central Frequency f_0, RMS Disturbance Torque M_s Applied to the Main Telescope Structure as a Function of the High Frequency Decay Rate of the Wind Tilt Excitation Normalized to 1 arcsec RMS[a]

Decay Rate	f_c (Hz)	σ_0 (arcsec/s^2)	f_0 (Hz)	RMS Torque M_s (N·m)
−8/3	13.3	17973	229	17
−11/3	5.6	748	27.7	0.71
−13/3	4.6	295	10.2	0.28
−17/3	3.85	115	2.4	0.11

[a]In all cases, the residual tilt is 0.07 arcsec RMS.

as a function of the assumed decay rate in the wind tilt excitation (Fig. 8); in all cases, the wind tilt excitation is 1 arcsec RMS and the control objective is a residual tilt of 0.07 arcsec RMS. The decay rate −17/3 of the atmospheric tilt has been added to the table for completeness. One observes that, if one sticks to the control objective of 0.07 arcsec, the RMS tilt acceleration σ_0 and the central frequency f_0 increase dramatically when the asymptotic decay rate of the wind tilt disturbance changes from −17/3 to −8/3.

The disturbance torque M_s applied to the telescope structure is obtained by multiplying the tilt acceleration by the moment of inertia I_a of M5; assuming a disk of diameter $D = 2.5$ m and mass $m_a = 500$ kg, $I_a = m_a D^2/16 = 195$ kgm^2. The RMS value of M_s is given in the last column of Table 1.

The problem may be examined in a slightly different way by leaving the compensator unchanged with $f_c = 4.6$ Hz(corresponding to the most frequently quoted decay rate of −13/3) and estimating the impact of the asymptotic decay rate (the various disturbance PSDs of Fig. 8, all normalized to 1 arcsec RMS). The results are presented in Table 2. The corresponding PSDs of the angular acceleration are given in Fig. 12.

One sees that, for a given control bandwidth, a lower decay rate of the wind disturbance will not only increase the residual tilt, but it will also significantly increase the disturbance torque applied to the telescope structure and broaden its frequency content. Let us now examine the effect of the disturbance torque generated by the wind compensation of the TTM control loop on the primary telescope structure.

Table 2. RMS Residual Tilt Error σ_e, RMS Tilt Acceleration σ_0, and Central Frequency f_0, RMS Disturbance Torque M_s Applied to the Main Telescope Structure for Various Values of the Asymptotic Decay Rate of the Wind Tilt Excitation (Normalized to 1 arcsec RMS)[a]

Decay Rate	Resid. Error σ_e (arcsec)	σ_0 (arcsec/s^2)	f_0 (Hz)	RMS Torque M_s (N · m)
−8/3	0.146	3229	67.2	3.05
−11/3	0.084	651	20.7	0.62
−13/3	0.07	295	10.2	0.28

[a]In all cases, the compensator has the same bandwidth, $f_c = 4.6$ Hz.

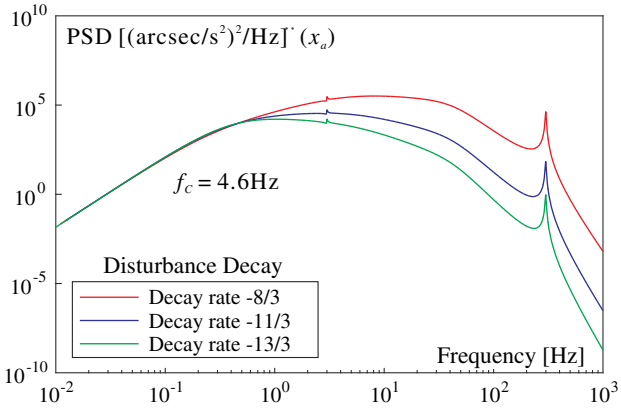

Fig. 12. PSD of the TTM angular acceleration for the three cases considered in Table 2. The compensator is the same in all cases ($f_c = 4.6$ Hz).

4. RESPONSE OF THE TELESCOPE STRUCTURE

A. Telescope Model

In order to estimate the impact of the reaction torque of the TTM (M5) on the telescope structure, a finite element (FE) model has been built based on the information available in Ref. [21] (Fig. 13); although not accurate, this model may be regarded as sufficiently representative of a 40 m telescope such as the E-ELT for the purpose of this discussion. The primary mirror consists of 714 independent segment units represented by a node array related to the upper surface of the truss system by springs; every node holds a lumped mass of 300 kg and has a single d.o.f. normal to the truss. The spring stiffness is such that the piston mode of the segments is 60 Hz. No tilt of the segments is allowed; they are considered as fully co-phased, in such a way that the surface of M1 is the best fit of the node displacements. The secondary mirror M2 is modeled as a lumped mass (12×10^3 kg) supported by the spider structure with only three degrees of freedom (piston, tip, tilt). The relay

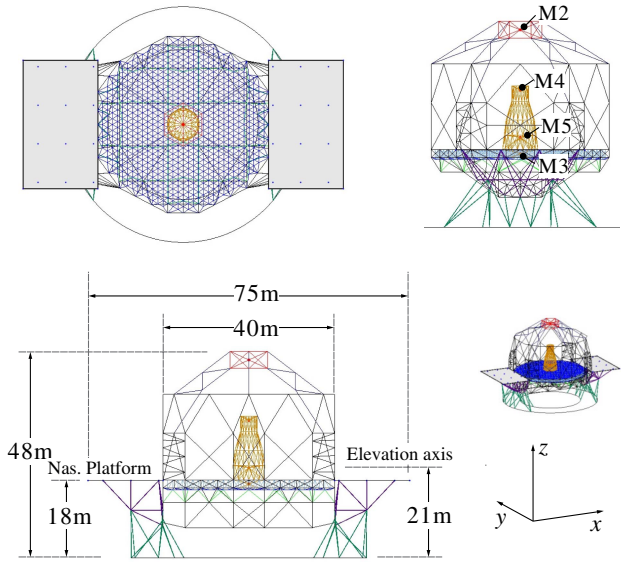

Fig. 13. Structural model of a 40 m class ELT telescope.

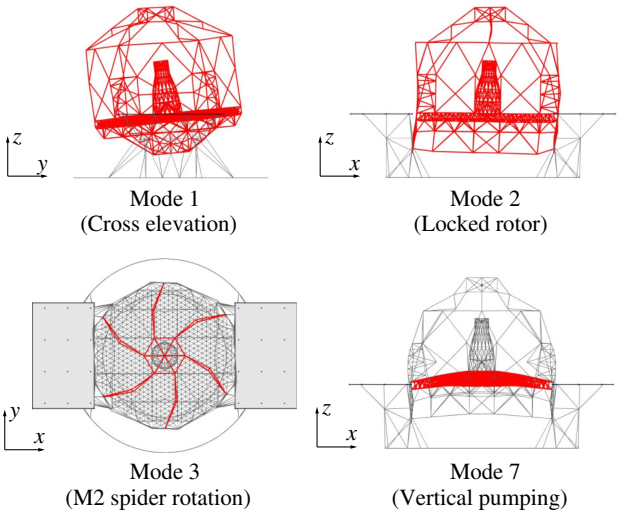

Fig. 14. Typical mode shapes: cross elevation modes ($f_1 = 3.04$ Hz), locked rotor mode ($f_2 = 3.17$ Hz), spider rotation mode ($f_3 = 3.4$ Hz), vertical pumping mode ($f_7 = 5.42$ Hz).

mirror M3, the deformable mirror M4, and the TTM M5 are modeled similarly with lumped masses of 12×10^3 kg, 2×10^3 kg, and 500 kg, respectively; they are mechanically connected with the tower structure, which is modeled as a truss. The altitude structure weighs 1500×10^3 kg and the center of gravity. height is 21 m. In the FE model, the truss system is modeled with beam elements with a tube cross section; the Nasmyth platform is modeled using Mindlin shell elements, and non-structural mass is added to obtain 95×10^3 kg on each side. The rotor drive is locked in the zenithal position.

The material is steel, and the modal damping is assumed to be 0.01 on all modes. The FE model has been developed in SAMCEF; details are available in Ref. [22]. A Craig-Bampton reduction has been performed to produce a reduced model of 1623 d.o.f. (including the 714 vertical displacements of the M1 segments). Figure 14 shows the first few global modes; the results seem to be in line with those available in Ref. [21]. The tip/tilt estimation requires only a few among the 1623 modes of the model; since the excitation consists

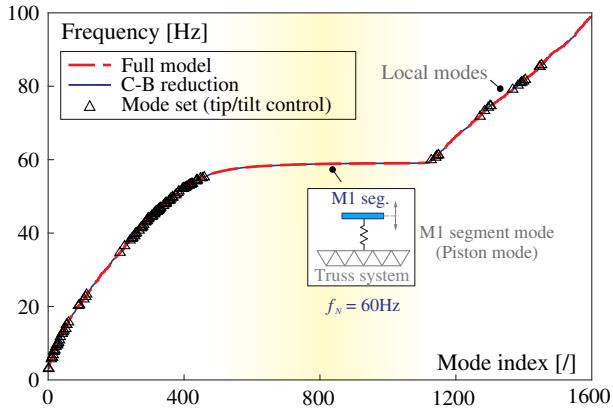

Fig. 15. Eigen frequency distribution of the telescope model. Full model, Craig-Bampton reduction, the modes selected for tip/tilt estimation are indicated by Δ.

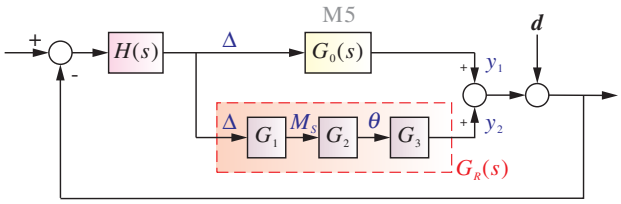

Fig. 16. Block diagram of the field stabilization loop. The upper branch $G_0(s)$ is the control of the TTM M5, while the lower branch $G_R(s)$ is the residual response of the telescope structure to the control torque of M5.

of two torques applied at M5 and we are interested in the tip/tilt responses of M2, M3, and M4, the mode selection is based on the numerical values of the residues (known as *modal flexibility* in structural dynamics) as follows:

$$\frac{\phi_i(M_5)\phi_i(M_k)}{\omega_i^2}, \tag{27}$$

where i is the index of the mode and ϕ_i is the mode shape normalized to a unit modal mass ($\mu_i = 1$). $\phi_i(M_5)$ and $\phi_i(M_k)$ stand for the rotation d.o.f. of M5 and M2 to M4, respectively; since one is interested into tip and tilt, 12 sets of modes are considered, and for each set, the 20 modes with the largest values of the modal flexibility are selected. This leads to a final choice of 135 modes (because of duplication) to evaluate

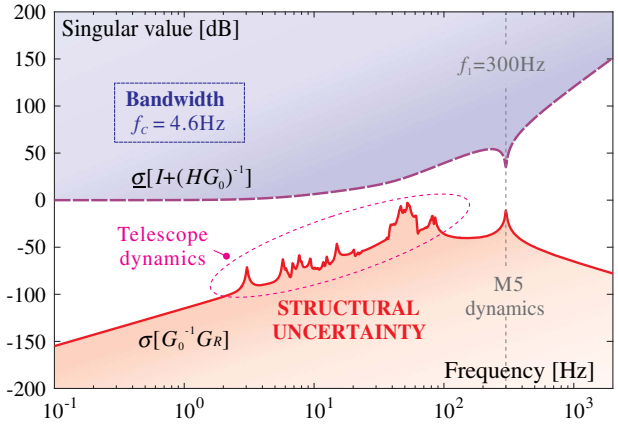

Fig. 17. MIMO stability robustness test (multiplicative uncertainty). A structural damping of 1% is assumed.

Table 3. Residual Tilt Error RMS Value σ_e (arcsec) and Central Frequency f_e (Hz)[a]

Decay Rate a	Bandwidth f_c (Hz)	σ_e (arcsec)	f_e (Hz)	σ_w (nm)	f_w (Hz)
−8/3	13.3	0.068	27.03	25.9	50.8
−8/3	4.6	0.146	18.52	6.21	49.1
−11/3	5.6	0.070	0.87	0.95	48.8
−11/3	4.6	0.084	0.85	0.66	48.3
−13/3	4.6	0.070	0.39	0.158	47.7

[a]M1 RMS wavefront error σ_w (nm) and central frequency f_w (Hz), for various values of the high frequency decay rate a of the wind tilt excitation (normalized to 1 arcsec) and various control bandwidth f_c.

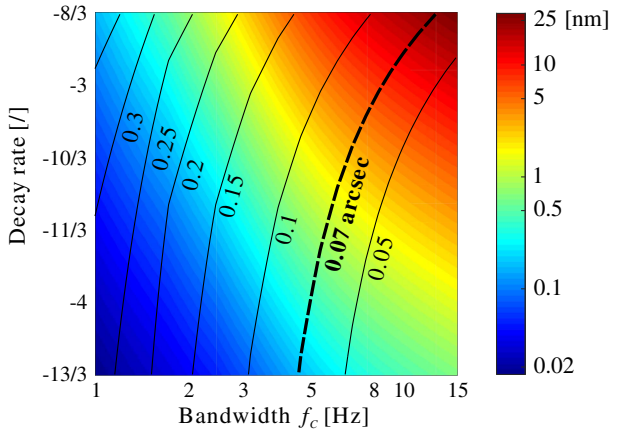

Fig. 18. Residual tilt error (iso lines, in arcsec) and M1 RMS wavefront error [color map, in nanometers (nm)] as a function of the wind tilt disturbance decay rate a and the control bandwidth f_c.

the telescope response. Figure 15 shows the eigen frequency distribution of the model. The modes involved in the tip/tilt estimation are highlighted.

B. Stability Analysis

Figure 16 shows the block diagram of the field stabilization loop. The M5 branch is 2×2, where the input Δ is the tip/tilt angular command of M5 and y_1 the contribution to the wavefront sensor. $G_0(s)$ are the M5 dynamics, including the optical amplification D_4/D_1 to bring y_1 to M1 level. The residual dynamics loop $G_R(s)$ contains the telescope dynamics. $G_1(s)$ relates the actuator command Δ to the disturbance torque M_s applied to the telescope structure, Eq. (24), $G_2(s)$ describes the dynamic response of the telescope (obtained from the FE model) leading to the tip/tilt angles θ of M1, M2, M3, and M4, and G_3 is the optical amplification. The overall tilt angle is obtained from the various components according to

$$\theta = \theta_1 - \theta_2 \frac{D_2}{D_1} + (\theta_3 - \theta_4 + \theta_5) \frac{D_4}{D_1}, \tag{28}$$

where D_2 is the diameter of the image of M1 on M2 and D_4 is the useful diameter of M4. d is a vector of two independent random processes distributed according to Fig. 8.

According to the stability theory of multi-input multi-output (MIMO) systems [23–25], a sufficient condition for stability is that

$$\overline{\sigma}(G_0^{-1} G_R) < \underline{\sigma}[I + (HG_0)^{-1}], \tag{29}$$

where $\overline{\sigma}$ and $\underline{\sigma}$ stand for the maximum and the minimum singular value, respectively. The result of this test is shown in Fig. 17, where a uniform modal damping of 1% has been assumed. One sees that there is a substantial stability margin.

Referring to Fig. 16, the closed-loop wind tilt response of the full system where the telescope model in the $G_R(s)$ branch

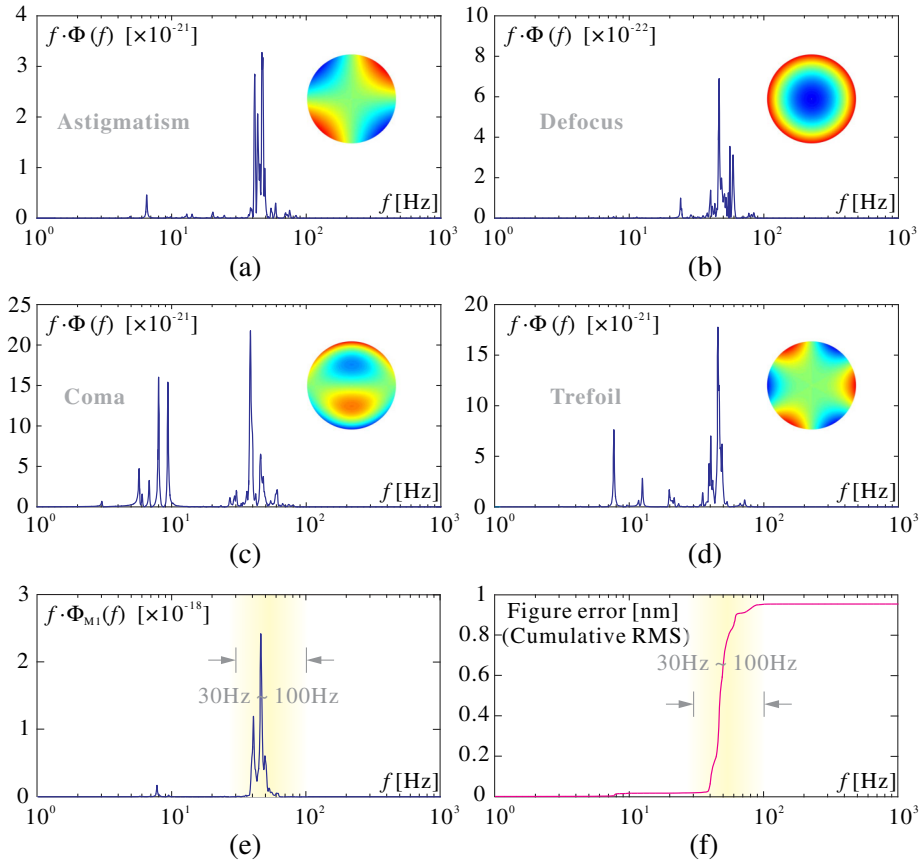

Fig. 19. Wavefront aberrations induced in M1 by the control torques of M5 in the case $a = -11/3$, $f_c = 5.6$ Hz. (a)–(d) PSD of various Zernike modes: astigmatism, defocus, coma, trefoil. (e) PSD of the wavefront error. (f) Cumulative RMS wavefront error.

includes 135 modes differs by less than 1% from that of the upper branch alone, when the dynamics of the telescope are neglected. This provides a clear justification for a decoupled design.

C. M1 Response to M5 Control Torques

According to the foregoing section, the telescope response cannot destabilize the tip/tilt control loop. However, the control torques M_s necessary to move M5 act as a disturbance to the telescope, and, as we have seen earlier, the spectral content of the disturbing torque depends strongly on the control bandwidth (measured by f_c) and on the high frequency attenuation rate a of the wind-shaking disturbance. The dynamic response of the primary mirror M1 may be estimated in two steps: (i) using the upper branch of Fig. 16 (M5) alone, the closed-loop control input Δ is calculated; (ii) using the lower branch of Fig. 16, the telescope response is computed in open loop, using the full model of the telescope, including 1600 modes. The surface figure of M1 is obtained by a least-squares fit of the 714 nodes representing the segments; the wavefront error is twice the mirror surface figure RMS error. The results are summarized in Table 3 for the set of values that have been considered earlier. Figure 18 displays the same information graphically for a wider range of values. In all cases, it has been observed that most of the energy in the signal is contained in the range of 30–100 Hz, as illustrated in Fig. 19 in the case ($a = -11/3$, $f_c = 5.6$ Hz); the figure shows the PSD of a few Zernike modes and the wavefront aberration (the representation $f\Phi(f)$ versus $\log f$ is used to give a fair representation of the energy content).

The foregoing analysis shows that if the target of a residual tilt error of 0.07 arcsec is to be met and the decay rate of the wind tilt disturbance is relatively low ($a > -3$), the wavefront aberration induced on M1 by the field stabilization control loop may become significant, with frequency components in the range 30–100 Hz, which may not be easy to eliminate by the adaptive optics control loop. In these circumstances, the residual tilt error (to be compensated for by M4) will have energy components at frequencies much higher than the atmospheric tilt (Fig. 2). Notice that values between −2 and −3 have been observed on Gemini South [20] (Fig. 4).

5. CONCLUSION

The analysis confirms the adequacy of a decoupled design of the field stabilization (M5) control loop. The small mass ratio between the M5 unit and the rest of the telescope supporting it makes the control-structure interaction unlikely, guaranteeing stability. However, the reaction torques necessary to control the tip/tilt mirror M5 have been found to depend critically on the asymptotic decay rate of the wind tilt disturbance. These torques act as a disturbance on the telescope structure, and, if the wind disturbance does not decay fast enough with the frequency ($a > -3$), it may generate significant wavefront errors in the primary mirror M1 in a frequency range (30–100 Hz) that may be difficult to eliminate by AO. Furthermore, the residual tilt error (to be compensated by M4) will have energy components at frequencies much higher than the atmospheric tilt.

APPENDIX A: ACCEPTANCE FUNCTIONS OF A 2D STRUCTURE

According to random vibration theory [19,26], if a structure is subject to a homogeneous random pressure field $p(\mathbf{x}, t)$, the PSD of the structural response $w(\mathbf{x}, t)$ at one point $\mathbf{x}$ is given by

$$\Phi_w(\mathbf{x}, f) \approx \sum_i \phi_i^2(\mathbf{x}) \cdot |H_i(f)|^2 . \Phi_p(f) \cdot A_{ii}(f), \qquad \textbf{(A1)}$$

where the sum extends to all the modes, $\phi_i(\mathbf{x})$ is the amplitude of the mode shape at $\mathbf{x}$, $H_i(f)$ is the transfer function of a single d.o.f. oscillator representing the modal amplification, $\Phi_p(f)$ is the PSD of the pressure at one point, and $A_{ii}(f)$ is the acceptance function of mode i

$$A_{ii} = \int_R \int_R \Psi_p(\mathbf{z}_1 - \mathbf{z}_2, f)\phi_i(\mathbf{z}_1)\phi_i(\mathbf{z}_2)\mathrm{d}\mathbf{z}_1\mathrm{d}\mathbf{z}_2, \qquad \textbf{(A2)}$$

where R is the entire structure area and $\Psi_p(\mathbf{z}_1 - \mathbf{z}_2, f)$ describes the spatial coherence of the pressure field; $\Psi_p(\mathbf{z}_1 - \mathbf{z}_2, f) = 1$ if it is fully correlated, $\Psi_p(\mathbf{z}_1 - \mathbf{z}_2, f) = \delta(\mathbf{z}_1 - \mathbf{z}_2)$ if it is completely spatially uncorrelated. If the coherence is isotropic, it depends only on the distance between the two points $\Delta z = |\mathbf{z}_1 - \mathbf{z}_2|$. Extending Davenport's result, Eq. (4), in two dimensions, the coherence is assumed to be

$$\Psi_p(\mathbf{z}_1 - \mathbf{z}_2, f) = \exp\left(-\frac{Cf}{U_m} \cdot \Delta z\right). \qquad \textbf{(A3)}$$

Figure 20 shows the acceptance functions A_{ii} as a function of the normalized frequency CLf/U_m of various modes with different boundary conditions (free-free and clamped on one side) of a square plate $L \times L$. The estimation has been done numerically with $C = 7$, $L = 40$ m, and $U = 10$ m/s. One sees that all the curves have the same asymptotic decay rate. In the particular case of a rigid body mode, ϕ_i is a constant, and one can write

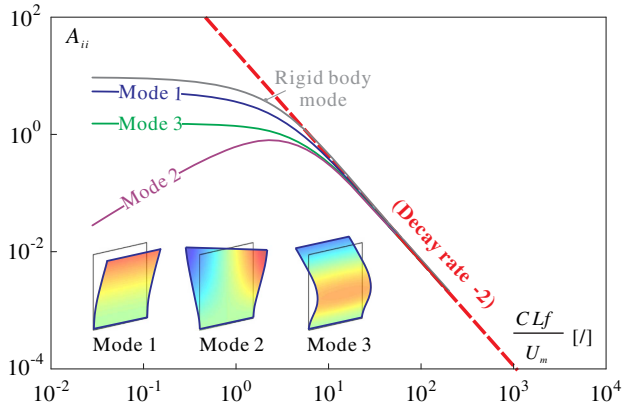

Fig. 20. Square plate subject to homogeneous, isotropic pressure field of coherence $\exp(-\frac{Cf}{U_m}\Delta z)$. Acceptance functions A_{ii} of various modes as a function of the normalized frequency CLf/U_m. The boundary conditions are rigid body and clamped on one side. All the curves have an asymptotic decay rate of −2.

$$A_{ii} \simeq \int_0^1 \int_0^1 \mathrm{d}x_1 \mathrm{d}y_1 \int_0^1 \int_0^1 \times \exp\left[-\alpha\sqrt{(x_1-x_2)^2+(y_1-y_2)^2}\right]\mathrm{d}x_2\mathrm{d}y_2 \quad \textbf{(A4)}$$

with the notation $\alpha = CLf/U_m$. When α is large, the decay of the exponential is so fast that the second integral becomes independent of (x_1, y_1), and the limits of integration may be extended to infinity, leading to

$$\int_{-\infty}^{\infty}\int_{-\infty}^{\infty} \exp\left(-\alpha\sqrt{x_2^2+y_2^2}\right)\mathrm{d}x_2\mathrm{d}y_2 \quad \textbf{(A5)}$$

Upon performing a change of variables, $x_2 = r\cos\theta$, $y_2 = r\sin\theta$, the integral may be transformed into

$$\int_0^{2\pi}\mathrm{d}\theta\int_0^{\infty} r\exp(-\alpha r)\mathrm{d}r = \frac{2\pi}{\alpha^2} = 2\pi\left(\frac{U_m}{CLf}\right)^2, \quad \textbf{(A6)}$$

which shows that the asymptotic decay rate is −2.

APPENDIX B: TWO-DEGREE-OF-FREEDOM MODEL

Referring to Fig. 6, the open-loop dynamics of the two-degree-of-freedom systems is governed by Newton's law as follows:

$$m_a\ddot{x}_a = F_a - c_a(\dot{x}_a - \dot{x}_s) - k_a(x_a - x_s),$$
$$m_s\ddot{x}_s = -F_a - c_a(\dot{x}_s - \dot{x}_a) - k_a(x_s - x_a) - c_s\dot{x}_s - k_s x_s,$$

or in matrix form using the Laplace variable s as

$$\begin{bmatrix} m_a s^2 + c_a s + k_a & -(c_a s + k_a) \\ -(c_a s + k_a) & m_s s^2 + (c_a + c_s)s + (k_a + k_s) \end{bmatrix} \times \begin{Bmatrix} x_a \\ x_s \end{Bmatrix} = \begin{Bmatrix} F_a \\ -F_a \end{Bmatrix}. \quad \textbf{(B1)}$$

By solving Eq. (B1), one can obtain the transfer functions between the mirror motions (x_a and x_s) and the actuation force F_a as follows:

$$\frac{x_a}{F_a} = \frac{m_s s^2 + c_s s + k_s}{(m_a s^2 + c_a s + k_a)[m_s s^2 + (c_a + c_s)s + (k_a + k_s)] - (c_a s + k_a)^2},$$
$$\frac{x_s}{F_a} = \frac{-m_a s^2}{(m_a s^2 + c_a s + k_a)[m_s s^2 + (c_a + c_s)s + (k_a + k_s)] - (c_a s + k_a)^2} \quad \textbf{(B2)}$$

From Eq. (6), it follows that the open-loop transfer function reads

$$\frac{y}{F_a} = \frac{-m_a s^2 + \delta(m_s s^2 + c_s s + k_s)}{(m_a s^2 + c_a s + k_a)[m_s s^2 + (c_a + c_s)s + (k_a + k_s)] - (c_a s + k_a)^2} \quad \textbf{(B3)}$$

Acknowledgment. Kainan Wang was supported by the China Scholarship Council.

REFERENCES

1. B. Delabre, "Optical design for an adaptive anastigmatic five-mirror extremely large telescope," Astron. Astrophys. **487**, 389–397 (2008).
2. M. Cayrel, "E-ELT optomechanics: overview," Proc. SPIE **8444**, 844418 (2012).
3. R. Gilmozzi and J. Spyromilio, "The 42 m European ELT: status," Proc. SPIE **7012**, 701219 (2008).
4. R. Biasi, M. Andrighettoni, G. Angerer, C. Mair, D. Pescoller, P. Lazzarini, E. Anaclerio, M. Mantegazza, D. Gallieni, E. Vernet, R. Arsenault, P.-Y. Madec, P. Duhoux, A. Riccardi, M. Xompero, R. Briguglio, M. Manetti, and M. Morandini, "VLT deformable secondary mirror: integration and electromechanical tests results," Proc. SPIE **8447**, 844710 (2012).
5. S. Esposito, A. Riccardi, L. Fini, A. T. Puglisi, E. Pinna, M. Xompero, R. Briguglio, F. Quirós-Pacheco, P. Stefanini, J. C. Guerra, L. Busoni, A. Tozzi, F. Pieralli, G. Agapito, G. Brusa-Zappellini, R. Demers, J. Brynnel, C. Arcidiacono, and P. Salinari, "First light AO (FLAO) system for LBT: final integration, acceptance test in Europe, and preliminary on-sky commissioning results," Proc. SPIE **7736**, 773609 (2010).
6. P. M. Hinz, A. Bouchez, M. Johns, S. Shectman, M. Hart, B. McLeod, and P. McGregor, "The GMT adaptive optics system," Proc. SPIE **7736**, 773612 (2010).
7. A. Preumont, R. Bastaits, and G. Rodrigues, "Scale effects in active optics of large segmented mirrors," Mechatronics **19**, 1286–1293 (2009).
8. E. Vernet, L. Jochum, P. La Penna, N. Hubin, R. Muradore, J. M. Casalta, I. Kjelberg, J.-C. Sinquin, F. Locre, P. Morin, R. Cousty, J.-M. Lurçon, J.-J. Roland, B. Crepy, E. Gabriel, R. Biasi, M. Andrighettoni, G. Angerer, D. Gallieni, M. Mantegazza, M. Tintori, E. Molinari, D. Tresoldi, G. Toso, P. Spanó, M. Riva, G. Crimi, A. Riccardi, G. Marque, J.-L. Carel, and E. Ruch, "The field stabilization and adaptive optics mirrors for the European extremely large telescope," Proc. SPIE **7015**, 701512 (2008).
9. J.-M. Conan, G. Rousset, and P.-Y. Madec, "Wave-front temporal spectra in high-resolution imaging through turbulence," J. Opt. Soc. Am. A **12**, 1559–1570 (1995).
10. T. Von Kármán, "Progress in the statistical theory of turbulence," Proc. Natl. Acad. Sci. USA **34**, 530–539 (1948).
11. A. G. Davenport, "The application of statistical concepts to the wind loading of structures," Proc. Inst. Civ. Eng. **19**, 449–472 (1961).
12. W. Gawronski, "Three models of wind-gust disturbances for the analysis of antenna pointing accuracy," The Interplanetary Network Progress Report IPN PR 42-149 (2002).
13. D. G. MacMynowski and T. Andersen, "Wind buffeting of large telescopes," Appl. Opt. **49**, 625–636 (2010).
14. G. Z. Angeli, M. K. Cho, M. Sheehan, and L. M. Stepp, "Characterization of wind loading of telescopes," Proc. SPIE **4757**, 475712 (2002).
15. M. Ravensbergen, "Main axes servo systems of the VLT," Proc. SPIE **2199**, 21999 (1994).
16. P. Bely, *The Design and Construction of Large Optical Telescopes* (Springer, 2006).
17. D. G. MacMynowski, K. Vogiatzis, G. Z. Angeli, J. Fitzsimmons, and J. E. Nelson, "Wind loads on ground-based telescopes," Appl. Opt. **45**, 7912–7923 (2006).
18. P. Bearman, "Wind loads on structures in turbulent flow," in *The Modern Design of Wind-Sensitive Structures* (1971), pp. 42–48.
19. M. Novak, "Random vibrations of structures," in *Proceedings of the Fourth International Conference on Applications of Statistics and Probability in Soil and Structural Engineering* (1983), pp. 539–550.
20. C. Kulcsár, G. Sivo, H.-F. Raynaud, B. Neichel, F. Rigaut, J. Christou, A. Guesalaga, C. Correia, J.-P. Véran, E. Gendron, F. Vidal, G. Rousset, T. Morris, S. Esposito, F. Quiros-Pacheco, G. Agapito, E. Fedrigo, L. Pettazzi, P. Clare, R. Muradore, O. Guyon, F. Martinache, S. Meimon, and J.-M. Conan, "Vibrations in AO control: a short analysis of on-sky data around the world," Proc. SPIE **8447**, 844714 (2012).
21. ESO, *E-ELT Construction Proposal* (European Southern Observatory, 2011).
22. K. Wang, "Piezoelectric adaptive mirrors for ground-based and space telescopes," Ph.D. thesis (Université Libre de Bruxelles, 2019).
23. J. Doyle and G. Stein, "Multivariable feedback design: Concepts for a classical/modern synthesis," IEEE Trans. Autom. Control **26**, 4–16 (1981).
24. J. M. Maciejowski, *Multivariable Feedback Design* (Addison-Wesley, 1989).
25. R. L. Kosut, H. Salzwedel, and A. Emami-Naeini, "Robust control of flexible spacecraft," J. Guid. Control. Dyn. **6**, 104–111 (1983).
26. A. Preumont, *Random Vibration and Spectral Analysis* (Springer, 1994).